Research Square

Preprints are preliminary reports that have not undergone peer review.
They should not be considered conclusive, used to inform clinical practice,
or referenced by the media as validated information.

Ultrafast and reproducible quantitative analysis of bacterial chemotaxis by microfluidic cell counting and imaging

Bing Fu

bingfu@cityu.edu.hk

City University of Hong Kong https://orcid.org/0000-0001-9952-2244

Chenwei Xiong

Article

Keywords:

Posted Date: November 3rd, 2026

DOI: https://doi.org/10.21203/rs.3.rs-11492736/v1

License: This work is licensed under a Creative Commons Attribution 4.0 International License.
Read Full License

Additional Declarations: There is **NO** Competing Interest.

Ultrafast and reproducible quantitative analysis of bacterial chemotaxis by microfluidic cell counting and imaging

Chenwei Xiong[a], Bing Fu[a#]

[a]Department of Biomedical Engineering, City University of Hong Kong, Hong Kong, Hong Kong SAR, China

#Address correspondence to Bing Fu: bingfu@cityu.edu.hk

Abstract

The capillary assay is a classical method for quantifying bacterial chemotaxis, but it relies on overnight plating and colony counting or optical density measurements, which are time-consuming and highly heterogeneous. Here, we developed an ultrafast chemotaxis quantification platform by coupling the capillary assay with automated microfluidic counting and imaging. This strategy preserves the simplicity and robustness of the conventional capillary assay while replacing overnight colony counting with rapid, real-time bacterial enumeration. We first characterized the microfluidic counting performance and validated its robustness across varying flow rates, sampling windows, and channel geometries. Then we successfully measured dose-dependent chemotactic behaviors towards classic chemo-attractants and chemo-repellents and discovered novel chemotaxis behavior towards metal gradients. Lastly, to further explore the possibility of eliminating the manual sample-transfer step, we designed and validated a proof-of-concept integrated microfluidic platform that combines chemotaxis, counting, and microscopic observation within a single device.

1. Introduction

Bacterial chemotaxis enables motile bacteria to move towards or away from chemical stimuli, playing a critical role in diverse biological processes, including host infection, biofilm formation, and nutrient foraging[1–3]. By directing movement towards favourable environment and avoiding harmful substances or stresses, chemotaxis enhances bacterial survival, growth and colony expansion[4]. For example, during host infection, bacteria must continuously navigate the highly heterogeneous chemical landscape of host tissues to locate nutrients, colonize specific niches, and evade host defenses, where chemotaxis is particularly important[5]. Therefore, understanding chemotactic signalling is essential for deciphering the fundamental mechanisms of pathogenesis, biofilm formation, and novel therapeutic targets identification.

Over the past several decades, a variety of population-level methods have been developed to investigate bacterial chemotaxis. These include the soft agar plate diffusion assay, which qualitatively assesses chemotaxis by observing halos of bacterial migration[1]; the border-crossing plate assay which monitors the expansion of motile cells towards or away from the agar releasing chemo-effectors[6]; and the U-shaped capillary assay, in which bacteria migrate from a suspension chamber into glass capillaries containing the test chemo-effector and the turbidity is evaluated[7,8]. Though widely used, many of these methods are either semi-

quantitative or suffer from large heterogeneity due to non-uniform surface, therefore are unable to detect subtle chemotaxis effect. Those limitations frequently create discrepancies between the results of different labs and prevent the easy discovery of novel chemo-effectors.

The capillary assay, introduced by Adler over five decades ago, is one convenient and low-cost way to reliably quantify chemotactic responses by measuring the accumulation of bacteria in a capillary containing attractants or repellents[9]. In this classic method, a sealed capillary filled with a test chemo-effector solution is inserted into a bacterial suspension. After incubation, the number of bacteria that have entered the capillary is determined by series of dilution followed by plating and manual colony counting after overnight growth, a labour-intensive and time-consuming procedure. Furthermore, only the endpoint information but not the real-time chemotactic response occurring in the capillary is captured.

An alternative approach is to directly count the bacteria without overnight culturing. Microfluidic technologies offer precise fluid control and single particle counting capability, making them attractive for ultrafast bacterial enumeration. Several microfluidic chemotaxis devices have been developed, including those that employ diffusion-based static gradients[10], laminar-flow interfaces[11], or hydrogel-embedded 3D matrices[12] to study bacterial migration at single-cell resolution. However, most existing devices rely on complex external pumps, intricate microchannel networks for gradient generation, and specialized fabrication facilities [13,14].

Here, we avoid sophisticated microscale gradient generation and focus on a simple and rapid counting method. Specifically, we couple the traditional capillary assay with a stand-alone microfluidic counter: after incubation, the capillary content is injected into the microfluidic counter for fast, reliable and automated counting. This offline approach preserves the accuracy and simplicity of the capillary assay while replacing overnight colony counting with real-time cell counting, reducing the readout time from >12 h to <5 min. As validation, we quantified the chemotactic responses of wildtype *E. coli* and a chemoreceptor-deficient mutant (*Δtar*) to the well-known chemo-attractant aspartate and chemo-repellent indole[8]. We also tested several metal ions and found that nickel and zinc act as effective novel chemo-effectors. This system is also shown to have large tolerance on geometry, flow rate and observation window, and generate more reproducible results compared to other traditional chemotaxis assays. Although the offline workflow substantially accelerates chemotaxis quantification, sample transfer between the capillary and the counter may introduce extra error and reduce reproducibility. To address this, we further designed and demonstrated a proof-of-concept integrated microfluidic platform in which the microchannel serves as both the chemotaxis region and the counting region, allowing real-time *in situ* observation. Altogether, our approach directly addresses the limitations of reproducibility, quantification and read-out speed of chemotaxis assays, resolving both population-level kinetics and single-cell heterogeneity during chemotactic behavior.

2. Results

2.1 Fabrication of the microfluidic counter

The microfluidic counter was fabricated using standard soft lithography and replica molding techniques. The device layout was designed in AutoCAD and printed as a high-resolution plastic film mask (Supplementary Figure 1a). A 3-inch silicon wafer was spin-coated with a negative photoresist to a target thickness of 50 μm, then pre-baked, exposed to UV light through the mask, post-baked, and developed to produce the master mold. Polydimethylsiloxane (PDMS) prepolymer mixed with curing agent at a 10:1 weight ratio was poured over the mold, degassed, and cured at 60 °C overnight. The cured PDMS slab was peeled off, and inlet/outlet ports were punched. Finally, the PDMS replica and a glass slide were treated with oxygen plasma and bonded irreversibly to form the sealed microchannel.

The counter consists of a single straight rectangular microchannel (length 10 mm) with a fixed width of 100 μm and a height of 40 μm in the standard configuration, although devices with heights of 20 and 80 μm and widths of 50 and 200 μm were also fabricated to evaluate geometric tolerance. The channel connects to an inlet port for sample injection and an outlet port linked to a syringe for waste collection (Supplementary Figure 1b).

2.2 Characterization and robustness of the microfluidic counter

A schematic of the imaging and counting region is depicted in Figure 1a, illustrating the flow direction, the microscope field of view, and the automated counting principle. The microscope focuses on the mid-plane of the channel ($z = 0$), where the laminar flow is. Bright-field videos are recorded at a fixed frame rate. In brief, bacteria are detected against the background and tracked across frames. The bacterium is counted when its centroid crosses the central counting line (Figure 1a). Full details of the detection, tracking and counting algorithm are provided in Supplementary Information section 2.

To systematically investigate how the geometries of device will affect counting results, we first performed COMSOL numerical simulations to characterize the flow-field velocity. Under a constant volumetric flow rate of 6 μL/h, the local fluid velocity displayed a classical laminar flow profile across the channel height (Figure 1b). As the channel height decreased from 80 μm to 20 μm, the maximum flow velocity at the channel center (height = 0) increased significantly from approximately 0.45 mm/s to 1.5 mm/s, resulting in a much steeper velocity gradient. The 2D velocity heatmaps illustrated the velocity distribution across the entire cross-section (100 μm width) for channel heights of 80 μm (Figure 1c), 40 μm (Figure 1d), and 20 μm (Figure 1e).

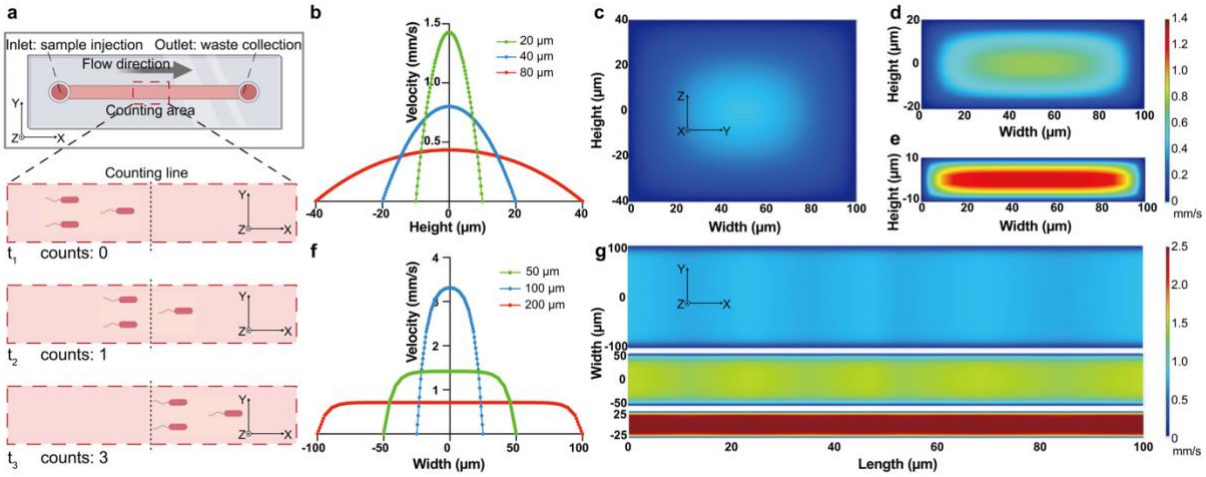


Figure 1. Numerical simulation of fluid velocity profiles and cross-sectional distributions within microfluidic channels. **(a)** Schematic illustration of the microfluidic counting with three-dimensional coordinate axes labelled to indicate the channel geometry. **(b, f)** Velocity profiles along the channel height direction for three different channel heights (20 μm, 40 μm, and 80 μm) **(b)** and three different channel widths (50 μm, 100 μm, and 200 μm) **(f)** under a constant volumetric flow rate. **(c-e)** Two-dimensional velocity heatmaps across the channel cross-sections (width = 100 μm) for channel heights of **(c)** 80 μm, **(d)** 40 μm, and **(e)** 20 μm. **(g)** Two-dimensional velocity heatmaps along the horizontal plane for channel widths of 200 μm, 100 μm, and 50 μm.

Numerical simulations on velocity profile along the channel height direction were further conducted to evaluate the influence of channel width variations (50, 100, and 200 μm) under a constant volumetric flow rate of 6 μL/h (Figure 1f). The fluid velocity distribution along the channel width axis varied significantly with geometric constraints. For the widest channel (200 μm), the profile exhibited a broad, relatively flat central plateau with a maximum velocity of approximately 0.6 mm/s. As the channel width was narrowed to 100 μm and further to 50 μm, the velocity profile transformed into a highly peaked parabolic shape, with the center velocity surging dramatically to approximately 1.4 mm/s and 3.3 mm/s, respectively. The two-dimensional velocity distribution heatmaps illustrated the flow along a 1000 μm channel length for widths of 200 μm, 100 μm, and 50 μm (Figure 1g). The transitions from low velocity (blue) to high velocity (dark red) clearly demonstrated that lateral confinement forces a substantial acceleration of the fluid, while maintaining a stable and uniform flow pattern throughout the longitudinal channel path.

These simulations define the hydrodynamic conditions that the counting algorithm must tolerate. As the channel height decreases, bacteria at the center cross the detection line more quickly. Conversely, the steeper gradient implies a larger velocity difference between the center and the wall, which could bias the spatial distribution of cells sampled by the detection line if bacteria preferentially swim in low-shear regions. Similarly, narrowing the channel width from 200 to 50 μm raises the centerline velocity from ~0.6 to ~3.3 mm/s and sharpens the parabolic profile, increasing the velocity contrast across the channel. Despite these variations, the

volumetric flow rate is constant, so the total number of bacteria passing through the cross-section per unit time is determined solely by the cell concentration and flow rate. Thus, as long as the counting algorithm can reliably detect every bacterium crossing the detection line, the absolute count should remain independent of channel geometry and flow velocity.

To validate the reliability of the microfluidic counting platform across different channel dimensions and flow rates, we first characterized the performance of the counter using *E. coli* suspensions of known OD values. At any fixed sampling window under the flow rate of 6 μL/h, the detected bacterial counts exhibited a strong linear correlation with the ground-truth cell concentrations ranging from 5.0×10^5 to 1.5×10^6 cells/mL (Figure 2a). Additionally, under a constant cell density, the counts increased linearly with the sampling window from 20 s to 240 s, where higher OD resulted significantly steeper slopes (Figure 2b). These results confirm that bacteria counts are proportional to both concentration and sampling window, and the readout remains linear across a large concentration range and sampling window.

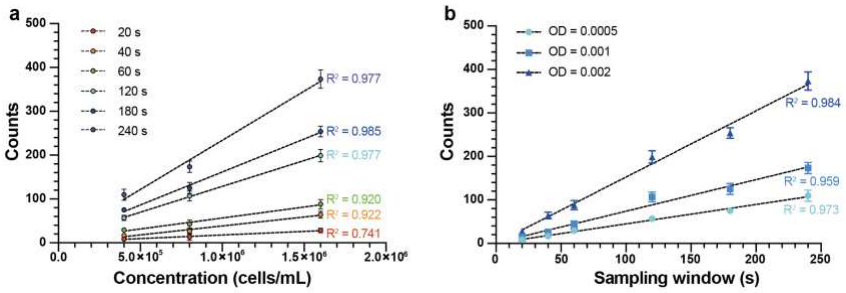


Figure 2. Evaluation of the offline counter performance using cell suspensions of known OD. **(a)** Total counts as a function of cell concentration under different sampling windows. **(b)** Total counts as a function of sampling windows across three different OD levels.

To validate the reliability of the microfluidic counter, the absolute counts were converted into colony-forming unit CFU (cells/mL) to assess the system stability across various operational parameters (Figure 3) according to the following equation:

$$CFU = \frac{1000 \times N}{Q \times t}$$

where *CFU* is the cell concentration (cells/mL), *N* is the absolute raw count detected during the sampling window, *Q* is the set flow rate (μL/h), and *t* is the sampling window (hours). For a low-concentration bacteria suspension (OD_{600} = 0.0068), raw counts scaled linearly with flow rates (2-10 μL/h, R^2 = 0.9881, Figure 3a), while the calculated cell concentration remained remarkably constant at approximately 4-5×10^6 cells/mL, consistent with the OD value (Figure 3b). Similarly, varying the sampling window (10-25 s) yielded linear raw counts (R^2 = 0.9901, Figure 3c) but a stable calculated CFU (Figure 3d). For an even lower concentration (OD_{600} = 0.0014), the calculated CFU remained stable around 0.8×10^6 cells/mL regardless of changes in flow rate (Figure 3e) or sampling window (Figure 3f), consistent with the expected OD. The

slight underestimation of cell concentrations likely originates from missing the cells above or below the observation focal plane.

Moreover, we tested the dynamic detection range of the counter. Within the higher concentration range of 1.0×10^5 to 1.2×10^6 cells/mL, the raw counts displayed an excellent linear correlation with the bacterial concentrations at flow rate 6 μL/h (Figure 3g). Lower concentration range of 8.0×10^3 to 1.2×10^5 cells/mL requires enhanced flow rate of 90 μL/h, where the linear relationship persisted (Figure 3h). The linearity assessment between OD_{600} concentration value and CFU value calculated from counts was also shown in Supplementary Figure 2.

Importantly, to directly test whether the hydrodynamic variations predicted by the simulations affect the counting accuracy, we evaluated devices with a range of channel dimensions. As established in the simulations, narrowing the channel width from 200 μm to 50 μm increases the velocity more than five-fold (from ~0.6 to ~3.3 mm/s), while reducing the channel height from 80 μm to 20 μm similarly raises the velocity from ~0.45 to ~1.5 mm/s and steepens the velocity gradient. These simulation results indicate that the fluid environment varies dramatically across different geometries. To experimentally test whether the counting system remains accurate under such widely varying flow conditions, we measured the calculated CFU readouts using microchannels of different heights (20, 40, and 80 μm, with fixed 100 μm width, Supplementary Figure 3a) and different widths (50, 100, and 200 μm, with fixed 40 μm height, Supplementary Figure 3b). In all cases, the CFU remained consistent with the expected cell concentrations, despite the large differences in velocity field. These steady readouts confirm that the system is able to tolerate diverse microfluidic scales without sacrificing performance.

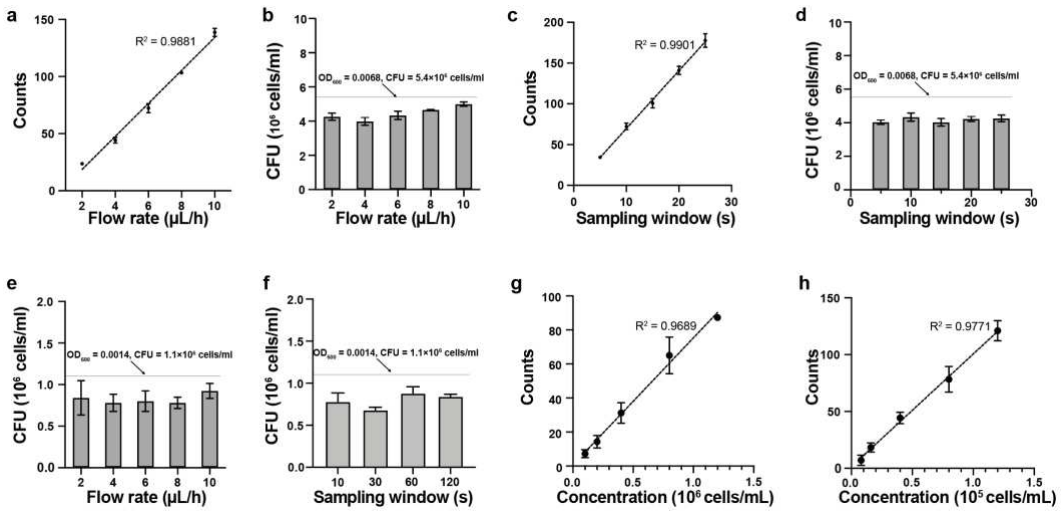


Figure 3. Validation of cell concentration readout. **(a-d)** Evaluation of flow rate and sampling window effect using a bacterial suspension of OD_{600} = 0.0068, CFU = 5.4×10^6 cells/mL. **(a)** Counts and **(b)** calculated CFU as a function of flow rate. **(c)** Counts and **(d)** calculated CFU concentrations as a function of sampling window. Ground truth CFU is indicated with a dashed line. **(e, f)** Evaluation of flow rate and sampling window effect using a lower concentration

suspension (OD_{600} = 0.0014, CFU = 1.1×10^6 cells/mL). CFU concentrations are shown across varying **(e)** flow rates, **(f)** time windows. **(g, h)** Linearity assessment at higher and lower concentration ranges.

Taken together, these results confirm that the microfluidic counter is robust against variations in flow rate, sampling window, and channel geometry. The calculated concentrations recover the ground truth and remain highly consistent across a 5-fold range of flow rates (2-10 μL/h) and a 12-fold range of sampling windows (10-120 s), for bacterial densities as low as 8.0×10^3 cells/mL. These properties are particularly beneficial for sensitive detection of chemotaxis behavior, which we explore in the following section.

2.3 Capillary assay with microfluidic counting for chemotaxis analysis

To validate the capability of our microfluidic counter for quantifying bacterial chemotaxis, we first performed capillary assays with the known chemo-attractant aspartate, sensed primarily by the Tar chemoreceptor[15]. After incubating in a reservoir containing bacteria for 45 minutes at 30 °C, the capillaries (containing aspartate or buffer) were carefully withdrawn, and their exterior surfaces were rinsed with buffer to remove any adhered bacteria, and the internal suspension was injected into the microfluidic counter for cell counting (Supplementary Figure 4 and 5). The chemotactic response was quantified as the fractional change in bacterial counts relative to the buffer-only control, defined as:

$$Change\ ratio = \frac{N_{chemo-effector} - N_{control}}{N_{control}}$$

where $N_{\text{chemo-effector}}$ is the number of bacteria counted in the capillary containing the chemo-effector, and N_{control} is the count from the buffer-only control capillary. This normalization eliminates heterogeneity of bacteria density in the reservoir and enables direct comparison across different experiments.

Number of wildtype *E. coli* exposed to aspartate of increasing concentrations exhibited a substantial accumulation in the capillary compared to the buffer-only control, confirming the attractant chemotaxis (Figure 4a, orange bars). For repellent response, indole, a well-characterized chemo-repellent for *E. coli*, was used. When WT cells were exposed to indole, we observed a dose-dependent reduction in capillary accumulation relative to the buffer control (Figure 4a, pink bars). These results established that our microfluidic counter captures both attractant and repellent chemotactic behaviors for well-characterized chemo-effectors.

We next investigated the unknown chemotactic responses of *E. coli* to various metal ions, for which emerging evidence suggests that Tar may also respond to[16]. We quantified the responses of both WT and *Δtar* strains (chemoreceptor Tar was knocked out) to nickel and zinc ions. For the WT strain, nickel (10 μM) acted as a potent repellent, causing a significant drop in bacterial accumulation below the baseline control (Supplementary Figure 6a). High-concentration zinc (1000 μM) similarly elicited a strong repellent response, whereas low-concentration zinc

(10 μM) triggered a slight elevation in counts, indicating mild attraction. For *Δtar* mutant, the repellent response to nickel was weakened, with the change ratio shifting from approximately −0.7 in WT to approximately −0.4 in *Δtar* (Figure 4b, Supplementary Figure 6b). In contrast, the responses to zinc showed no statistically significant differences between WT and *Δtar* (Figure 4b). This indicates that the Tar receptor plays an active role in mediating repulsion towards nickel but is not involved in sensing zinc.

To evaluate the sensitivity and reproducibility of our microfluidic counter against the conventional colony counting method, we compared the two approaches with 0.5 mM aspartate. While the conventional colony counting did not resolve a statistically significant difference between the chemo-effector and control groups, the microfluidic counter revealed a substantially more profound difference (Figure 4c). Notably, beyond the substantial time saving, the microfluidic counting approach significantly reduced data heterogeneity compared to conventional colony counting and soft agar assay (Supplementary Figure 7a). Irregular colony spreading (second plate of 0.2 mM indole) often happens due to uncontrollable drops on the non-uniform agar surface. Consequently, the coefficient of variation for the microfluidic counter (~0.1) is approximately similar to or 2.5 to 5-fold lower than that of the traditional plating method under various conditions (Figure 4d). This reduced variability improves the ability to distinguish subtle chemotactic responses from experimental noise, thereby increasing the effective sensitivity of the assay to small changes in chemotactic behavior.

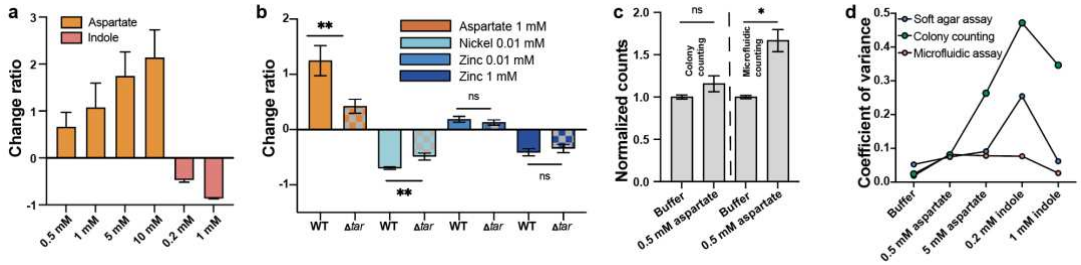


Figure 4. Evaluation of attractant and repellent chemotactic behavior in WT and *Δtar E. coli* using offline microfluidic counter. **(a)** Quantitative chemotactic change ratios for WT *E. coli* strains under aspartate attracting or indole repelling condition. **(b)** Quantitative chemotactic change ratios normalized against the blank baseline, evaluating the phenotypic divergence between WT and Δ*tar* under different chemical environments. **(c)** Direct comparison of the offline microfluidic counter and colony-counting-based quantification of the chemotactic response to 0.5 mM aspartate. **(d)** Coefficient of variance calculated for different approaches.

These results indicate that the offline microfluidic cell counter can accurately resolve both attracting and repelling chemotactic responses within capillary assay, making it a robust tool for studying bacterial chemotactic behaviors.

2.4 Integrated capillary assays coupled with microfluidic counting

We further explore whether the step of manual sample transfer from capillary to counter could be eliminated by integrating the chemotaxis migration process in the counting device. We

developed an integrated microfluidic device consisting of PDMS microchannel (length 10 mm, width 200 µm, height 40 µm) bonded to a glass substrate, with one open end connected to a reservoir (2 mm × 5 mm) containing 50 µL bacterial suspension (Figure 5a). The microchannel serves both as the capillary for chemotaxis migration and the counting region for in-situ enumeration. In contrast to the offline mode, the integrated device operates entirely under static, flow-free conditions. For each experiment, the microchannel was pre-filled with either chemotaxis buffer (control) or chemo-effector solution (experiment), followed by the reservoir loaded with 50-µL bacterial suspension. The device was then placed on an inverted microscope stage, and time-lapse bright-field images were acquired downstream the reservoir–channel interface with 5 min interval over 60 min. Bacteria continuously swim into the buffer-filled channel even in the absence of any test chemicals, attributed to random bacterial diffusion from high cell density. The cell density in the microchannel increased progressively from 0 to 60 min, visually confirming active bacterial swimming. Crucially, within the microchannel, *E. coli* exhibited unconstrained, free random swimming completely undisturbed by fluidic flow, as captured in Supplementary Movie 1. Additionally, the absence of directional bulk flow at the interface was verified (Supplementary Movie 2, Supplementary Figure 8a), in contrast to bacteria disturbed by the flow (Supplementary Movie 3, Supplementary Figure 8b). Numerical simulations confirmed that the fluidic velocity in the integrated device was zero (Supplementary Figure 9), ensuring that bacterial accumulation in the microchannel originated from active bacterial motility rather than bulk fluid flow. Bacterial counting and trajectory reconstruction were performed using a custom-developed MATLAB-based image analysis package (Supplementary Information section 2).

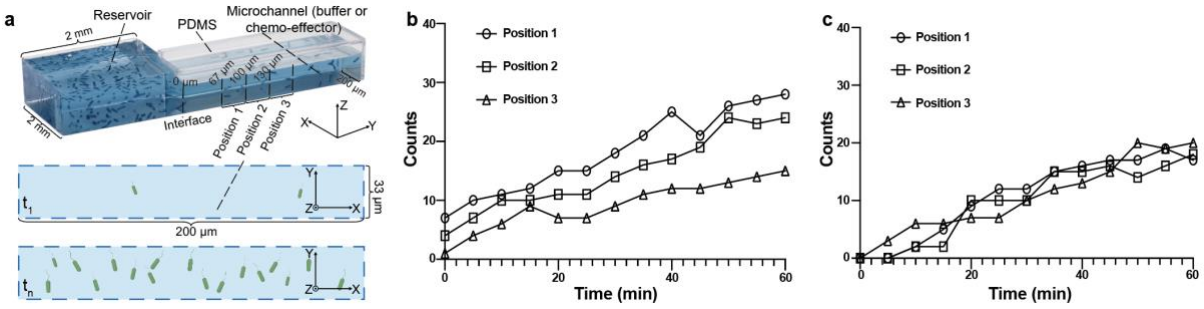


Figure 5. Real-time monitoring of bacterial migration behavior within an integrated microfluidic platform. **(a)** Schematics of integrated device. **(b)** Absolute bacterial counts recorded over a 60-min interval at three adjacent spatial locations (Positions 1, 2, and 3, located at 67 µm, 100 µm, and 133 µm downstream the reservoir-microchannel interface, respectively). **(c)** Relative bacterial counts over time across the same three positions, demonstrating excellent spatial uniformity in chemotactic bacterial accumulation.

Having established this undisturbed baseline, quantitative enumeration was executed at three adjacent positions (67, 100, and 133 µm) downstream from the interface (Figure 5b). In the buffer control, bacteria continuously swam into the microchannel of the integrated device. All three positions exhibited a robust, synchronized increase in absolute bacterial counts over 60

minutes. Positions closer to the reservoir edge exhibited slightly higher initial counts due to their immediate proximity to the cell source. Upon normalizing the baseline variations, the relative accumulation curves for the three spatial positions tightly overlapped (Figure 5c). This indicates a highly uniform and steady bacterial swimming through the microchannel, driven purely by active bacterial motility.

These results indicate that the integrated microfluidic device can successfully resolve microscale bacterial migration with high spatial precision. By transitioning from continuous-flow counting after collecting bacteria from capillary assay to *in situ* and real-time counting in the microchannel, the platform eliminates the needs of washing away test chemicals or bacteria outside the capillary, and provides an undisturbed, flow-free microenvironment for studying real-time chemotactic behavior. The counting result shows that the device is highly reliable for evaluating bacterial motility, establishing a solid baseline control for subsequent chemotactic response analyses.

Following the evaluation of the bacterial random motility in buffer, we then examined the chemotactic response to the chemo-attractant aspartate. Representative time-lapse images showing the progressive accumulation of WT cells responding to 1 mM aspartate at the 100 μm position are presented in Figure 6a. First, we utilized numerical simulation to confirm that the chemical concentration gradient can be established and stabilized at the microchannel-reservoir interface within 5 minutes (Supplementary Figure 10). When exposed to aspartate, WT strain demonstrated a significant dose-dependent chemotactic response (Figure 6b blue curves). At 10 mM aspartate, the relative counts of WT cells inside the microchannel increased rapidly, exceeding the count in the buffer control (~130 vs. ~30 counts at 45 min, dark blue vs. light blue curves). At a lower concentration of 1 mM aspartate, WT cells still exhibited a clear yet weaker chemotaxis compared to the buffer control. In sharp contrast, the Δ*tar* mutant, which lacks the specific Tar chemoreceptor for aspartate, showed minimal chemotactic response where the count accumulation curves of 1 mM or 10 mM aspartate and buffer control are largely similar (Figure 6b red curves).

To more quantitatively evaluate the chemotaxis behavior, the change ratio of area under the curve relative to the respective buffer baseline was calculated at different time points (Figure 6c, Supplementary information section 1.3). For 10 mM aspartate gradient, WT cells showed a dramatic and statistically significant increase in change ratio, reaching >2.5 at 40 to 60 min (the plateau phase). Conversely, the Δ*tar* mutant exhibited a ratio near 0.2 across all time timepoints. A similar, though smaller, significant difference between WT and Δ*tar* was observed at 40 min and 60 min under the 1 mM aspartate gradient condition, corroborating the receptor-specific bacterial chemotactic migration.

Comparison between WT and Δ*tar* indicates that the increased bacterial accumulation observed in the channel is driven primarily by active, receptor-mediated chemotaxis rather than random diffusion. Importantly, the integrated platform provides continuous kinetic information that is inaccessible to the offline device. Notably, significant accumulation of WT cells in response to

10 mM aspartate was observable as early as 10 minutes (Figure 6c), indicating cells display chemotactic response very early. Thus, the readout speed is further increased compared to the offline system, which requires 45-min incubation followed by sample transfer and counting. Altogether, the integrated mode reduces the total assay time while eliminating sample transfer steps and minimising operational losses and experimental variability. This feature is particularly advantageous when fast chemotaxis determination is required.

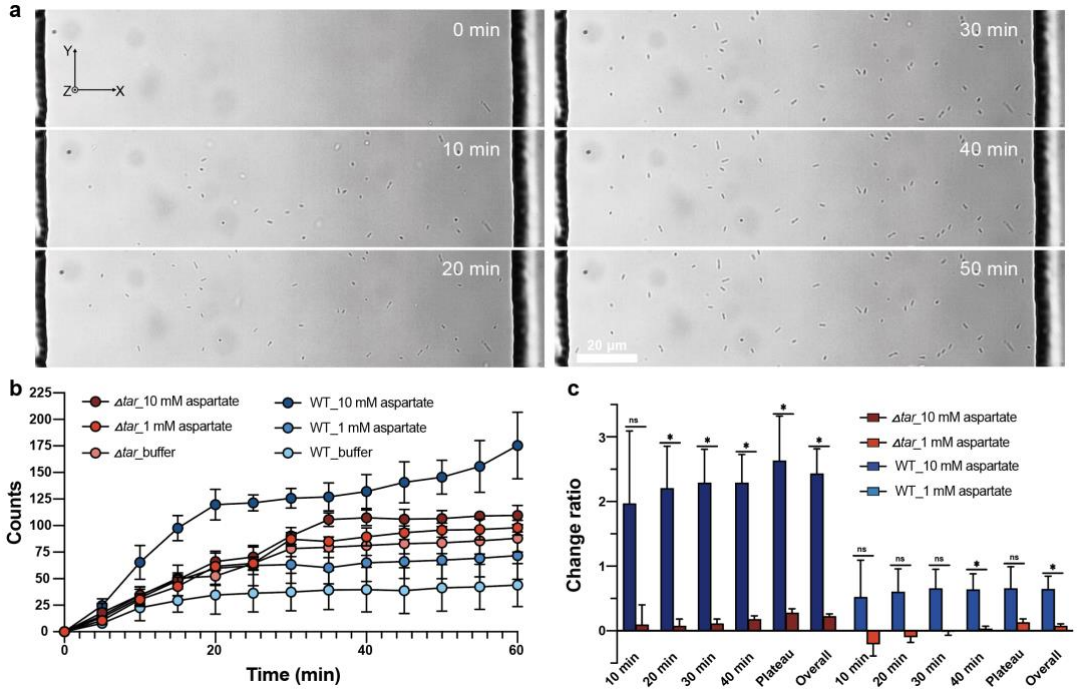


Figure 6. Quantitative analysis of chemo-receptor-mediated *E. coli* chemotaxis using integrated microfluidic device. **(a)** Sequential time-lapse microscopic images demonstrating the progressive accumulation of bacteria (WT responding to 1 mM aspartate) within the ROI located 100 μm away from the reservoir–microchannel interface at 0, 10, 20, 30, 40, and 50 min. **(b)** Time-dependent relative counts of WT and Δ*tar* strains entering the microchannel under exposure to buffer, 1 mM aspartate, or 10 mM aspartate over a 60-min duration. **(c)** Change ratios of bacterial accumulation (by calculating area under curve) relative to their respective buffer controls at distinct time points (10, 20, 30, 40 min), the plateau phase (40-60 min), and across the overall duration.

In addition, the integrated device enables real-time single-cell tracking during chemotaxis. We mapped individual bacteria trajectories (4 min duration) and quantified their movement 5 min after mixing the bacteria in the reservoir with the solution in the microchannel (Figure 7). Plotting the migration trajectories of *E. coli* revealed a directional bias toward the microchannel containing 10 mM aspartate (Figure 7b), as compared to the buffer control (Figure 7a). To quantify this directional preference, we calculated the chemotaxis index (CI) for individual cell trajectories. The CI is defined as the net displacement projected onto the gradient direction divided by the total accumulated path length. Thus, a positive CI indicates net migration toward the gradient, whereas a negative CI indicates migration in the opposite direction, with larger

absolute values reflecting stronger directional preference. Bacteria moving along the aspartate gradient exhibited a higher directionality, with a mean CI value of approximately 0.08, compared to the CI value of 0.05 in buffer control (we attribute it to the diffusive migration due to cell density difference).

In summary, the integrated device provides a proof-of-concept for rapid, real-time chemotaxis analysis, reliably detecting chemotactic responses as early as 10 min after gradient exposure – substantially faster than the offline workflow. Moreover, continuous monitoring captures the temporal evolution of chemotactic responses, providing information that is inaccessible with endpoint measurements.

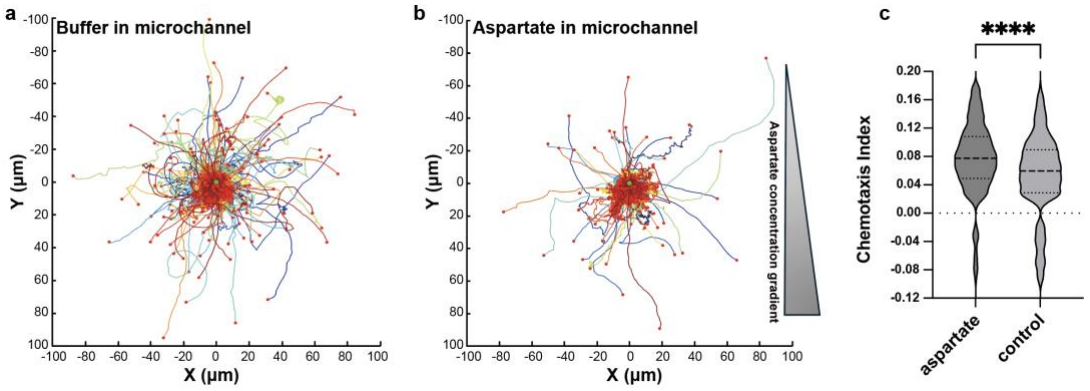


Figure 7. Single-cell tracking and chemotactic behavior analysis using integrated microfluidic device. **(a, b)** Bacterial migration trajectories of individual cells plotted from a common origin. The green points mark the starts, and the red points mark the ends. All starting points have been re-plotted to overlap at (0,0). **(c)** Quantitative comparison of the chemotaxis index under aspartate gradient and control conditions.

3. Conclusions

In this study, we successfully established an ultrafast, quantitative chemotaxis assay by coupling the classical capillary method with a microfluidic counter. The microfluidic platform enabled automated enumeration of *E. coli* within minutes, reducing the readout time from overnight culturing to seconds or minutes. Through systematic validation across flow rates, sampling windows, and channel geometries, we showed that the counter delivers consistent bacteria concentration readouts down to 8.0×10^3 cells/mL, with substantially improved reproducibility compared to traditional plating. Using this offline system, we resolved dose-dependent attractant responses to aspartate and repellent responses to metals ions, including Tar-dependent repulsion by nickel.

As an exploratory extension, we developed an integrated device where the microchannel itself served as both the migration and counting region, allowing real-time, *in situ* observation of bacterial accumulation without additional manual sample transfer. This integrated design provided continuous cell count information and captured significant chemotactic responses as

early as 10 minutes. Beyond population-level chemotaxis, this mode enables single-cell trajectory mapping, revealing directional movement along attractant gradients.

Crucially, both the offline and integrated modes prioritize simplicity in device design and rapid readout, whereas the integrated mode additionally offers unique advantages for mechanistic studies requiring high temporal resolution, spatial mapping, or single-cell analysis. Together, they constitute a versatile toolkit that addresses the major limitations of existing chemotaxis assays, e.g. readout speed and reproducibility. When compared with other methodologies (Table 1), our platforms are highly quantitative and much faster, replacing labour-intensive overnight plating with faster, automated counting. The design of the device is simple and easily achievable in a regular wet lab, without requiring complex photolithography facility. The integrated mode further distinguishes itself by capturing real-time bacteria trajectories with minimal equipment (requiring only a standard microscope and no external pump), which is a significant practical advantage over many complicated microfluidic chemotaxis devices.

Collectively, coupling the classical capillary assay with microfluidic counting provides a robust and ultrafast approach for quantitative chemotaxis measurements. The proof-of-concept integrated device further demonstrates the potential to extend this approach toward all-in-one platforms for real-time, *in situ* analysis of bacterial chemotaxis.

Method	Readout	Assay time	Ease of implementation	Reproducibility	Real-time
Soft agar expansion[1]	Halo diameter	Days	High (Petri dish)	Low (nonuniform agar surface)	No
Border-crossing plate assay[6]	Expansion front area	Days	High (Petri dish)	Low (nonuniform agar surface)	No
Capillary assay[17]	CFU after dilution and plating	~ 12 hours	Medium (labour-intensive dilution)	Medium (dilution variance)	No
Microfluidic gradient chips[10,12]	Tracking via transmission or fluorescence microscopy	Minutes to hours	Low (complex facilities and intricate fabrication)	High (controlled gradient and flow)	Yes
Offline capillary and microfluidic counter (this work)	Single-cell counting	An hour	Medium (microscope and pump)	High (capillary, controlled flow)	No
Integrated capillary-counter chip (this work)	In-situ real-time counting	Minutes to an hour	High (microscope, no other facilities required)	High (chip-based, minimal handling)	Yes

Table 1. Comparison of different bacterial chemotaxis quantification methodologies.

4. Materials and Methods

4.1. Bacterial strains and growth conditions

E. coli and its mutant *Δtar* strains were grown overnight (18 h) in LB medium on a shaker at 250 rpm and 37 °C. Then 50 μL of the overnight culture were added to 5 mL fresh LB and grown to exponential phase (4 h, 250 rpm, 37 °C). Cells were harvested, washed, and resuspended in chemotaxis buffer to an $OD_{600} \approx 0.05$ (~5×10^7 cells/mL).

4.2. Capillary assay

Capillary assays were conducted to assess the chemotactic responses of *E. coli* to specific attractants and metal ions, such as aspartate and nickel. This classic method involved placing capillaries containing attractants in a bacterial suspension and measuring the resulting bacterial accumulation into the capillaries over time like the setup we used in the Supplementary Figure 4.[9,17] Before conducting the capillary assay, strains were grown overnight (18 h) in LB medium on a rotator shaker at 250 rpm and 37 °C. The overnight cultured cells (5 µL) were then added to fresh LB solution (5 mL) and cultured to exponential phase (250 rpm and 37 °C, for 4 h). Subsequently, 200 µL aliquots of bacterial suspension (OD ~ 0.075) were placed into the wells of a 24-well plate. One end of a capillary was then inserted into the chemo-attractant/repellent solution with certain concentration. After the capillary was filled with the chemo-effector solution, one end was sealed by fire. The other end of the capillary went through the rubber adaptor and got immersed into the bacterial suspension. After incubation for 45 min, the capillaries were removed from the plate, and the portion of the capillary that was in contact with bacteria suspension was rinsed with water. The contents were emptied into a microcentrifuge tube and then injected into the offline microfluidic device under constant flow for quantification.

4.3. Offline microfluidic counter and integrated device

Both the offline microfluidic counter and the integrated microfluidic device were fabricated using photoresist patterning, development, and bonding[18]. The device layout was initially designed using AutoCAD and printed as a plastic film mask. For chip fabrication, a 50-µm-thick layer of photoresist (SU8-3025, Microchem) was spin-coated onto a 3-inch silicon wafer. Following a prebaking step at 95 °C for 20 min, photolithography was performed under UV light. The wafer was then post-baked at 95 °C for 8 min and developed to obtain the patterned structure. The resulting silicon mold was stored in a petri dish. A polydimethylsiloxane (PDMS) mixture (Dow Corning SYLGARD 184) was prepared by thoroughly mixing the precursor and curing agent at a weight ratio of 10:1. The PDMS mixture was poured onto the mold and cured at 60 °C overnight. The cured PDMS was then peeled off from the mold and cut into individual slabs. Inlet and outlet ports were created using a custom-made hole puncher. Finally, the PDMS slabs were bonded to glass slides (100 µm thick) with the aid of oxygen plasma treatment.

The offline microfluidic counter consisted of a straight channel with an inlet and outlet (Supplementary Figure 1). Bacterial suspension was driven through the channel at controlled flow rates using a syringe pump. The region of interest (ROI) focused on the center of the channel; a video was recorded at each condition, and the number of bacteria passing a fixed counting line was counted using ImageJ and customized MATLAB scripts.

In the integrated microfluidic device, the microchannel was filled with attractant or buffer solution. The open end was immersed into a 50-µL bacterial suspension in a custom-made well (2 mm × 5 mm). After 60 min incubation at 37 °C, the device was placed on a microscope, and bacteria were counted in a fixed ROI. The integrated device was tested for *E. coli* chemotactic behavior under 1 mM and 10 mM.

4.4. Numerical simulation procedure

The numerical simulations were performed using COMSOL Multiphysics (version 5.6) based on the finite element method to investigate the fluid velocity profiles within the microfluidic channels. To evaluate how microchannel geometry and flow rate affect the velocity field and counting performance, the simulation of pressure-driven laminar flow was conducted in the offline microfluidic counter. Additionally, the flow simulation in the integrated microfluidic device was conducted to verify the absence of bulk fluid flow. For both simulations, a physics-controlled mesh with refined boundary layers near the walls was employed; the maximum element size was set to 2 μm in the bulk and 0.5 μm near the walls.

In the offline microfluidic counter, the microfluidic channel geometry was modelled as a rectangular domain with a fixed length of 1000 μm and a width varying across 50, 100, and 200 μm, while the channel height was independently varied among 20, 40, and 80 μm. A constant volumetric flow rate was imposed at the inlet, and the outlet was set to zero pressure. The no-slip boundary condition was applied to all channel walls. The fluid was assumed to be incompressible and Newtonian, with the laminar flow interface solving the incompressible Navier–Stokes equations. The model settings were described in Supplementary Figure 11 and Supplementary Table 1.

The integrated device consisted of a reservoir (2 mm × 5 mm) connected to a microchannel (10 mm × 200 μm). No external volumetric flow rate was applied and the open boundary was set to zero pressure. The simulation confirmed that the velocity magnitude remained zero throughout the domain, verifying that bacteria accumulation in the microchannel originated from active bacterial motility rather than bulk fluid flow. The model settings were described in Supplementary Figure 9 and Supplementary Table 2.

Acknowledgements

We thank Qiqi Hao, Xiaoming Zhu, Chenming Lu, and Hanfei Gu (City University of Hong Kong) for helpful discussions. We thank Linghan Zhang and Bee Luan Khoo (City University of Hong Kong) for the use of pump. This work was supported by the startup grant of City University of Hong Kong (Project No. 9610649), the National Natural Science Foundation of China (Project No. 32400163), and the Research Grants Council of the Hong Kong Special Administrative Region, China (Project No. CityU 21303824).

Data Availability

The source data for plotting main text Figures 1-7, Supplementary Figures 2, 3, 6, 7, 10 are compiled in the file Supplementary Data.xlsx. Other data are available from the corresponding author on reasonable request.

Author Contribution

C.X. and B.F. designed research; C.X. performed experiments and analyzed data; B.F. supervised the research and acquired funding; C.X. wrote the first draft of the manuscript; C.X. and B.F. wrote and revised the manuscript.

Reference

(1) Adler, J. Chemotaxis in Bacteria. **1966**, *153*.
(2) Wadhams, G. H.; Armitage, J. P. Making Sense of It All: Bacterial Chemotaxis. *Nat Rev Mol Cell Biol* **2004**, *5* (12), 1024–1037. https://doi.org/10.1038/nrm1524
(3) Cremer, J.; Honda, T.; Tang, Y.; Wong-Ng, J.; Vergassola, M.; Hwa, T. Chemotaxis as a Navigation Strategy to Boost Range Expansion. *Nature* **2019**, *575* (7784), 658–663. https://doi.org/10.1038/s41586-019-1733-y
(4) Keegstra, J. M.; Carrara, F.; Stocker, R. The Ecological Roles of Bacterial Chemotaxis. *Nat Rev Microbiol* **2022**, *20* (8), 491–504. https://doi.org/10.1038/s41579-022-00709-w
(5) Matilla, M. A.; Krell, T. The Effect of Bacterial Chemotaxis on Host Infection and Pathogenicity. *FEMS Microbiology Reviews* **2018**, *42* (1). https://doi.org/10.1093/femsre/fux052
(6) Partridge, J. D.; Harshey, R. M. Investigating Flagella-Driven Motility in Escherichia Coli by Applying Three Established Techniques in a Series. *JoVE* **2020**, No. 159, 61364. https://doi.org/10.3791/61364
(7) Yang, L.; Chen, X.; Zeng, X.; Radosevich, M.; Ripp, S.; Zhuang, J.; Sayler, G. S. Surface-Adsorbed Contaminants Mediate the Importance of Chemotaxis and Haptotaxis for Bacterial Transport Through Soils. *Front. Microbiol.* **2019**, *10*, 2691. https://doi.org/10.3389/fmicb.2019.02691
(8) Tso, W.-W.; Adler, J. Negative Chemotaxis in *Escherichia Coli*. *J Bacteriol* **1974**, *118* (2), 560–576. https://doi.org/10.1128/jb.118.2.560-576.1974
(9) Adler, J. A Method for Measuring Chemotaxis and Use of the Method to Determine Optimum Conditions for Chemotaxis by Escherichia Coli. *Journal of General Microbiology* **1973**, *74* (1), 77–91. https://doi.org/10.1099/00221287-74-1-77
(10) Kim, S.; Masum, F.; Kim, J.-K.; Chung, H. J.; Jeon, J. S. On-Chip Phenotypic Investigation of Combinatory Antibiotic Effects by Generating Orthogonal Concentration Gradients. *Lab Chip* **2019**, *19* (6), 959–973. https://doi.org/10.1039/C8LC01406J
(11) Mao, H.; Cremer, P. S.; Manson, M. D. A Sensitive, Versatile Microfluidic Assay for Bacterial Chemotaxis. *Proc. Natl. Acad. Sci. U.S.A.* **2003**, *100* (9), 5449–5454. https://doi.org/10.1073/pnas.0931258100
(12) Li, B.; Qiu, Y.; Glidle, A.; McIlvenna, D.; Luo, Q.; Cooper, J.; Shi, H.-C.; Yin, H. Gradient Microfluidics Enables Rapid Bacterial Growth Inhibition Testing. *Anal. Chem.* **2014**, *86* (6), 3131–3137. https://doi.org/10.1021/ac5001306
(13) Englert, D. L.; Manson, M. D.; Jayaraman, A. Flow-Based Microfluidic Device for Quantifying Bacterial Chemotaxis in Stable, Competing Gradients. *Appl Environ Microbiol* **2009**, *75* (13), 4557–4564. https://doi.org/10.1128/AEM.02952-08
(14) Inatomi, K.-I.; Izuo, S.-I.; Lee, S.-S. Application of a Microfluidic Device for Counting of Bacteria. *Lett Appl Microbiol* **2006**, *43* (3), 296–300. https://doi.org/10.1111/j.1472-765X.2006.01953.x
(15) Ortega, Á.; Zhulin, I. B.; Krell, T. Sensory Repertoire of Bacterial Chemoreceptors. *Microbiol Mol Biol Rev* **2017**, *81* (4), e00033-17. https://doi.org/10.1128/MMBR.00033-17

(16) Englert, D. L.; Adase, C. A.; Jayaraman, A.; Manson, M. D. Repellent Taxis in Response to Nickel Ion Requires Neither Ni^{2+} Transport nor the Periplasmic NikA Binding Protein. *J Bacteriol* **2010**, *192* (10), 2633–2637. https://doi.org/10.1128/JB.00854-09

(17) Han, G.; Cooney, J. J. A Modified Capillary Assay for Chemotaxis. *Journal of Industrial Microbiology* **1993**, *12* (6), 396–398. https://doi.org/10.1007/BF01569670

(18) Xiong, C.; Zhang, B.; Zhang, R.; Liu, Y. An Experimental and Numerical Study of Polyelectrolyte Hydrogel Ionic Diodes: Towards Electrical Detection of Charged Biomolecules. **2021**, 12.

Supplementary Files

This is a list of supplementary files associated with this preprint. Click to download.

- SupplementaryMovie1.avi
- ChemotacticcapillaryassaymicrofluidiccounterSIfinal.pdf
- SupplementaryMovie3.avi
- SupplementaryMovie2.avi
- SupplementaryData.xlsx